Niobium near-surface composition during nitrogen infusion relevant for superconducting radio-frequency cavities

G. D. L. Semione[1,2,*] A. Dangwal Pandey,[1] S. Tober,[1,2] J. Pfrommer,[1] A. Poulain,[3] J. Drnec,[3]
G. Schütz,[4] T. F. Keller,[1,2] H. Noei,[1] V. Vonk,[1] B. Foster,[1,2,5] and A. Stierle[1,2]

[1]*Deutsches Elektronen-Synchrotron DESY, D-22607 Hamburg, Germany*
[2]*Fachbereich Physik, Universität Hamburg, D-20355 Hamburg, Germany*
[3]*European Synchrotron Radiation Facility, 71 avenue des Martyrs, CS 40220, Grenoble Cedex 9, France*
[4]*Max Planck Institute for Intelligent Systems, Heisenbergstrasse 1, D-70569 Stuttgart, Germany*
[5]*University of Oxford, Keble Road, OX1 3RH, Oxford, United Kingdom*

A detailed study of the near-surface structure and composition of Nb, the material of choice for superconducting radio-frequency accelerator (SRF) cavities, is of great importance in order to understand the effects of different treatments applied during cavity production. By means of surface-sensitive techniques such as grazing incidence diffuse x-ray scattering, x-ray reflectivity, and x-ray photoelectron spectroscopy, single-crystalline Nb(100) samples were investigated *in* and *ex situ* during annealing in an ultrahigh vacuum as well as in nitrogen atmospheres with temperatures and pressures similar to the ones employed in real Nb cavity treatments. Annealing of Nb specimens up to 800 °C in a vacuum promotes a partial reduction of the natural surface oxides (Nb_2O_5, NbO_2, and NbO) into NbO. Upon cooling to 120°C, no evidence of nitrogen-rich layers was detected after nitrogen exposure times of up to 48 h. An oxygen enrichment below the Nb-oxide interface and posterior diffusion of oxygen species towards the Nb matrix, along with a partial reduction of the natural surface oxides, was observed upon a stepwise annealing up to 250 °C. Nitrogen introduction to the system at 250 °C promotes neither N diffusion into the Nb matrix nor the formation of new surface layers. Upon further heating to 500 °C in a nitrogen atmosphere, the growth of a new subsurface Nb_xN_y layer was detected. These results shed light on the composition of the near-surface region of Nb after low-temperature nitrogen treatments, which are reported to lead to a performance enhancement of SRF cavities.

I. INTRODUCTION

Superconducting radio-frequency (SRF) cavities are the foundation of modern particle accelerators and free-electron lasers (e.g., FLASH and EU-XFEL in Hamburg, Germany). Achieving higher accelerating gradients and better efficiency, as well as increasing their performance for continuous wave (cw) operation provides several challenges ranging from fundamental science up to large-scale production [1–3]. Recently, thermal treatments performed at high (800 °C–900 °C) and low (120 °C–160 °C) temperatures and involving nitrogen presence were reported to improve the quality factor (Q_0—the ratio of energy stored in a cavity to the energy lost per rf cycle) up to 3 times when compared with a regularly produced cavity [2,3].

However, an understanding of the processes involved and the parameters required is still elusive.

As a type-II superconductor, niobium (Nb) has the highest critical temperature and critical field among all pure elements. Combined with its resistance to corrosion and ductility, Nb has become the material of choice for SRF-based technology. The concentration of impurities (hydrogen, oxygen, nitrogen, and carbon) within the rf penetration layer (≈ 40 nm for pure Nb) is believed to be the key factor regarding the performance of cavities, either by lowering the electron mean-free path [4] and energy gap [5] or by trapping potential hydrogen which can cluster and precipitate niobium hydrides upon cooldown [6,7]. Traditionally, Nb-based SRF cavities were subjected to several production steps, including different polishing cycles like buffered chemical polishing (BCP) and electrochemical polishing (EP), as well as heat treatments at 800 °C and 120 °C [1,8] in a high vacuum in order to lower the hydrogen content inherent to the material [9]. In recent years, controlled annealing of SRF cavities in nitrogen atmospheres, at either high or low temperatures for

different time spans, showed a decrease in their surface resistance [2,3]. The former treatment, known as nitrogen doping, includes annealing polycrystalline Nb cavities for a few minutes at 800 °C in 3×10^{-2}–8×10^{-2} mbar of N_2. Such treatment conditions lead to the formation of β-Nb_2N inclusions at the surface as well as promoting the growth of NbO [6,10]. By etching approximately 5 μm by EP, therefore removing the aforementioned inclusions, cavities displayed record-breaking quality factors at intermediate accelerating field gradients up to 20 MV/m. Another treatment, called nitrogen infusion, consists in annealing Nb cavities at 800 °C for 3 h in a high vacuum (10^{-7}–10^{-6} mbar) followed by a decrease in temperature to the range 120 °C–200 °C. Subsequently, nitrogen is injected at a pressure of 3×10^{-2} mbar. The system is then kept in such conditions for 48 h, yielding cavities with quality factors in the range of 6×10^{10} and accelerating gradients up to 45 MV m^{-1} without the need of material removal [2]. Low-temperature annealing of Nb cavities under a N_2 atmosphere is therefore an intense topic of research, since operation at high accelerating gradients (>25 MV m^{-1}) with high Q_0 are necessary for potential upgrades of existing accelerators into cw operation, like the European x-ray free-electron laser (EU-XFEL), as well as the development of future particle accelerator projects. However, insights on the actual surface state during and after such treatments are lacking. Ideally, the knowledge obtained from model systems (e.g., single-crystal surfaces) can potentially be applied to real cavity materials and eventually lead to the discovery of new cavity treatments that will improve the performance limits.

Most of the studies found in the literature address N and Nb interactions at high temperatures [11–14]. Nonetheless, few reports detail investigations of Nb single crystals under low N_2 pressures and of cavity-grade Nb after undergoing real cavity-treatment conditions. Exposure of an oxide-free Nb(100) surface to N_2 pressures in the range 7×10^{-8}–7×10^{-7} mbar at around 345 °C leads to the formation of a NbN(100) epitaxial layer, while exposure at room temperature formed NbN clusters at the surface [15]. For polycrystalline cavity-grade Nb, nanoscale niobium-nitride islands were reported after heat treatments between 120 °C and 160 °C with a N_2 pressure of $\sim 3 \times 10^{-2}$ mbar, while photoelectron measurements displayed the presence of $NbN_{(1-x)}O$ below the natural oxide layer. Secondary ion mass spectrometry (SIMS) measurements revealed a diffusion of oxygen species for ~ 20 nm, while nitrogen diffused ~ 50 nm, having the highest concentration in the first few nanometers when the exposure temperature was 140 °C [16], which, however, contradicts the bulk diffusion lengths of oxygen in Nb reported in the literature [17]. In order to obtain further detailed crystallographic information about the near-surface dissolution of nitrogen and oxygen in pure Nb, we have investigated single crystals. By using such well-defined crystals, we address the intrinsic

properties of Nb, which will be modified by the presence of large-angle grain boundaries and other defects as present in real rf cavity material. Nevertheless, the results of our study on more idealized samples will add to our basic understanding of niobium's properties and serve as input for future studies on polycrystalline materials.

In this study, we investigated *in* and *ex situ* the effects of the recently proposed nitrogen infusion treatment in the near-surface region of Nb as well as the effect of stepwise annealing in UHV up to 500 °C in a nitrogen atmosphere by means of x-ray reflectivity (XRR), x-ray photoemission spectroscopy (XPS), high-energy grazing-incidence diffuse x-ray scattering (GIXRD), and scanning electron microscopy (SEM). High-photon-energy experiments facilitated the monitoring of changes within the few-nanometer to submicron depth from the surface. A gradual dissolution of Nb_2O_5, NbO_2, and NbO layers at the surface upon annealing, followed by oxygen diffusion into Nb, allied with the lack of evidence of nitrogen diffusion in infusion and higher-temperature treatment is discussed.

II. EXPERIMENTAL METHODS

A. Samples

Mechanically polished niobium (100) samples (10 mm diameter, 2 mm height) oriented to better than 0.1° were employed for this study. Unless stated otherwise, the samples were annealed at 2000 °C for 6 h by induction heating in an ultrahigh vacuum (UHV) at a starting pressure of $\sim 10^{-10}$ mbar and unavoidably exposed to air for several days before the experiments. This procedure ensures that the Nb single crystals are as clean as possible in the bulk.

B. Characterization techniques and experimental setups

A four-circle and a six-circle [18–20] diffractometer with Mo-K_α and Cu-K_α sources, respectively, were employed for *in situ* x-ray reflectivity measurements of the 800 °C annealed and nitrogen-infused samples. The stepwise annealing of the specimens was carried out at beam line ID31 at the European Synchrotron Radiation Facility (ESRF) in Grenoble, France, and followed by *in situ* high-energy GIXRD and XRR measurements using a photon energy of 70 keV, while the data were collected using two separate 2D pixel detectors. The use of high photon energies provides fast access to large areas in reciprocal space, excluding the need of a time-consuming sample and detector movements [21,22].

For all aforementioned studies, the samples were mounted in a dedicated UHV setup, allowing direct measurements at different temperatures and gas conditions. The chamber has a cylindrical beryllium window and is connected to a pumping system capable of reaching base pressures of $\sim 10^{-8}$ mbar without bakeout. The sample is heated by a tungsten filament (see Fig. 1) typically

achieving pressures of $\sim 10^{-7}$ mbar at 800 °C. For all experiments involving the presence of nitrogen, nitrogen gas (99.999% purity) was inserted in the chamber through a leak valve until the system reached a pressure of 3.3×10^{-2} mbar, after which all the valves were closed and the chamber was kept under a static nitrogen atmosphere.

Oxygen and nitrogen, residing at interstitial crystallographic sites in the Nb lattice, give rise to distinct x-ray diffuse scattering peaks by locally distorting the host lattice [23]. The concentration of these interstitials scales linearly with the diffusely scattered x-ray intensities. Because of refraction and absorption effects, the x-ray penetration into the Nb crystal is finite. When the incident angle α_i of the x-ray beam with respect to the surface is aligned from close to the critical angle for total external reflection, α_c, up to several times this value, the x-ray penetration can be steered from several nanometers up to micrometers [24]. The value of α_c depends on the electron density of the crystal and the x-ray energy. For the experiments presented here, $\alpha_c = 0.045°$, which puts stringent demands on the stability and precision of the diffractometer [22]. In a symmetric way, the exit angle of the scattered x rays also defines the penetration depth. In a GIXRD experiment, depth-resolved information is thus obtained by tuning the incident and exit angles of x rays whereby the so-called scattering depth Λ [25,26] is set. The experimental setup in grazing-incidence geometry is depicted in Fig. 1. X rays impinge on the surface of the sample under an incident angle α_i, and the diffracted signals are recorded by a large 2D detector.
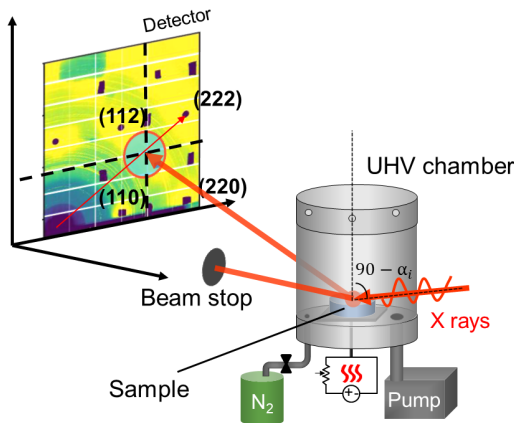

FIG. 1. Schematic of the GIXRD setup. The high-energy x-ray beam falls on the sample surface at grazing incident angle α_i, and the diffraction patterns are obtained by a 2D detector while the sample undergoes different annealing treatments under UHV and N_2. The blue circle represents the position of the interstitial diffuse scattering along the [111] direction (red line), while Nb reflections, indexed by their *hkl* values, are blocked with lead pieces to locally protect the detector. In order to sample 3D reciprocal space, the sample is typically rotated around its surface normal (dashed line), and at each angular position a diffraction pattern is recorded.

2D detector. Locally, the detector is shielded by lead (Pb) for the intense Bragg reflections of bulk Nb in order to avoid overexposure and damage.

XPS measurements were carried out separately using a lab-based system with monochromatic AlK_α radiation, and the spectra were recorded in fixed transmission mode with an energy resolution of 0.4 eV [20]. A high-resolution field-emission SEM was employed to characterize the surface morphology of the specimens.

III. RESULTS AND DISCUSSION

A. 800 °C anneal in UHV

During standard cavity preparation, an 800 °C annealing in a high vacuum is performed for a few hours to lower the inherent hydrogen content in the material acquired during manufacturing [1,27]. The presence of hydrogen can lead to the formation of niobium hydrides at the cavity surface, especially during the cooldown phase, leading to a poor performance [9]. A comparison between *in situ* XRR measurements of an "as-received" sample (without prior annealing) at room temperature and after 800 °C annealing for 1 h at 10^{-7} mbar as well as the derived electron density profiles are shown in Figs. 2(a) and 2(b), respectively. At room temperature, the natural oxide layer can be described best (from surface to the metal-oxide interface) using a three-layer model composed of Nb_2O_5, NbO_2, and NbO, with individual thicknesses of 2.90, 0.60, and 1.20 nm, respectively (error bar of ±0.1 nm) [28]. The total thickness of the natural oxide layer is 4.71 nm, while the roughness varies from 0.2 to 0.4 nm for the oxide-metal interfaces while being close to 1.25 nm for the vacuum-Nb_2O_5 interface. After annealing to 800 °C, both Nb_2O_5 and NbO_2 layers reduced completely in favor of a 1.03-nm-thick NbO layer, while the interface roughness between NbO and Nb increased to 0.82 nm.

It is important to note here that the surface of Nb is not oxide-free after such an annealing, in contrast to what is reported in Ref. [2], but a NbO layer remains at the surface. A simulated oxide-free Nb surface is shown in Fig. 2(a), with clearly visible differences when compared to the collected data after annealing to 800 °C. Similar effects were observed for XRR measurements with the Nb(110) surface, where NbO was the only natural oxide remaining after annealing at 300 °C in UHV for 50 min, forming an epitaxial (111)-oriented NbO layer [28]. The transition from $Nb_2O_5/NbO_2/NbO$ upon annealing into NbO was also previously confirmed by XPS characterization [28]. Moreover, Auger spectroscopy revealed that clean Nb surfaces could be achieved only after annealing from 1800 °C to 2000 °C [29], in agreement with the high-resolution STM studies of similarly prepared Nb surfaces [30].

For the (100) surface, XPS measurements on single-crystalline Nb etched by BCP and annealed at around 155 °C and 265 °C in UHV showed predominantly a
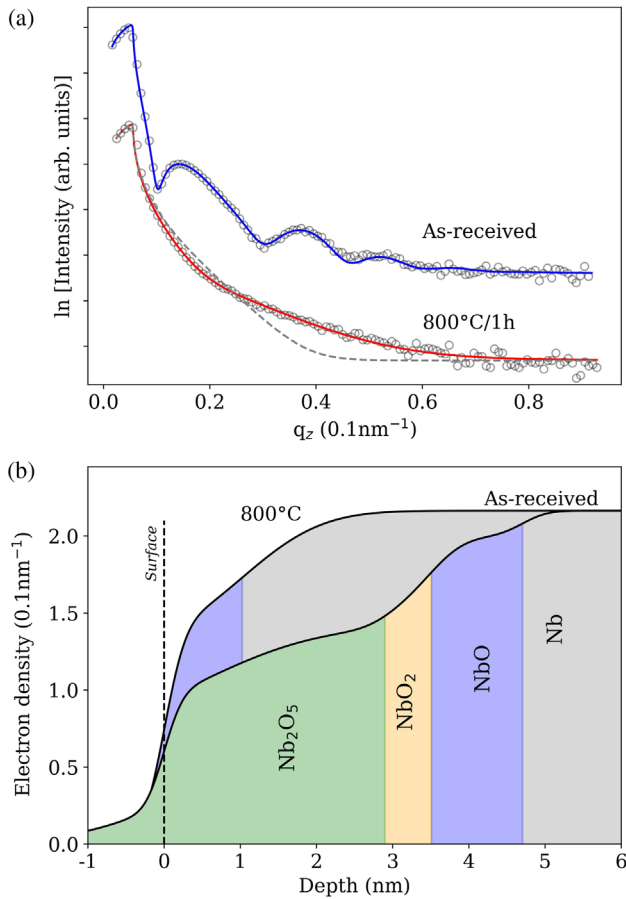
FIG. 2.   (a) X-ray reflectivity data measured with Mo K_α radiation (open circles) with respective fits (solid lines) for a Nb(100) single crystal as received and after 800 °C annealing in UHV for 1 h. The dashed line represents the simulated curve for a Nb surface without any surface oxide and with a constant background. The scans are offset in the *y* direction for better visibility. (b) Electron-density profiles for both sets of data obtained from the fits.

transition from Nb_2O_5 and NbO_2 to Nb_xO ($0.4 < x < 2$), together with an increase in surface roughness [31]. Furthermore, the presence of epitaxial NbO was confirmed by means of GIXRD for cavity-grade Nb (100) specimens annealed at 900 °C in a high vacuum and treated with nitrogen at the same temperature [10].

Knowing that the release of oxygen by Nb in UHV does not occur below 1600 °C [17], it can be concluded that the available oxygen from the partially dissolved natural oxide layer diffuses into the Nb matrix. As will be shown later, for lower annealing temperatures, oxygen diffusion into Nb was confirmed by grazing-incidence x-ray diffuse scattering measurements, similar to what was observed for the (110) surface [28].

B. Nitrogen infusion

In order to achieve high quality factors ($Q_0 \sim 6 \times 10^{10}$) with accelerating gradients up to 45 MV m^{-1}, cavities are

subjected to the so-called infusion process, which consists of the aforementioned 800 °C anneal in a high vacuum followed by a decrease in the temperature to 120 °C, at which point nitrogen was introduced into the system, maintaining a constant pressure of 3.3×10^{-2} mbar (25 mTorr) for 48 h [2]. Figures 3(a) and 3(b) show *in situ* XRR data measured at each step of the infusion treatment as well as the fitted electron density profiles. At room temperature, before the treatment, the surface displays a similar configuration to the "as-received" sample, with the natural oxides following the order Nb_2O_5, NbO_2, and NbO from the surface to the metal-oxide interface. Individual thicknesses of 1.27, 0.17, and 1.14 nm for Nb_2O_5, NbO_2, and NbO, respectively, were extracted from the fit. All interfaces showed roughness between 0.1 and 0.4 nm. All fits of this sample show a discrepancy in the first few data points due to the surface curvature and faceting
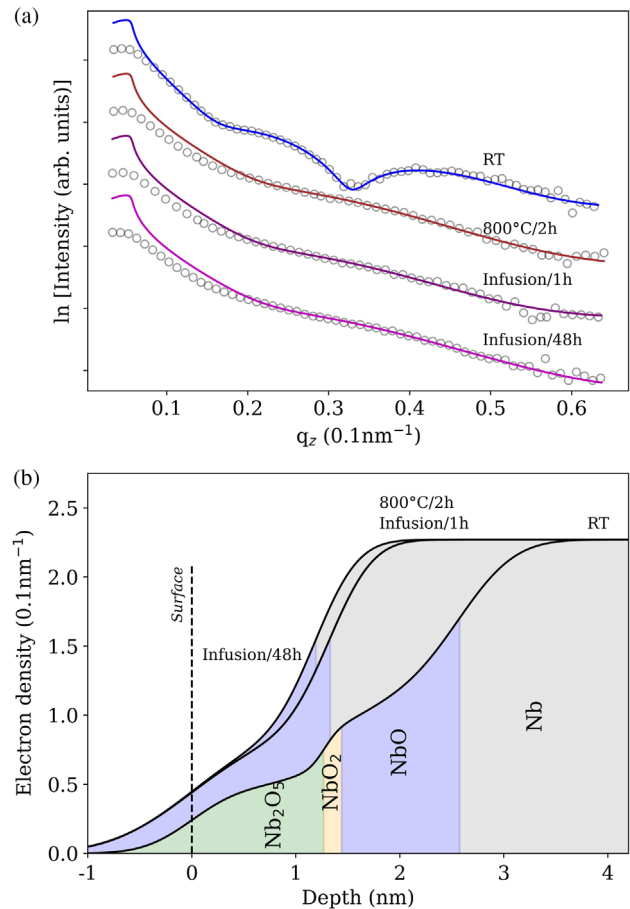

FIG. 3.   (a) X-ray reflectivity data measured with CuK$_\alpha$ radiation (open circles) with respective fits (solid lines) for various steps of the infusion procedure. The sample curvature compromises the fit in the first few data points. The scans are offset in the *y* direction for better visibility. (b) Electron density profiles for each step. The extracted densities are lower than the expected bulk values for the niobium oxides and metallic niobium due to the pronounced sample curvature.

caused by the 2000 °C anneal performed prior to the x-ray experiments [32].

Upon annealing at 800 °C for 2 h, similar to the previous results, the surface was composed of a single NbO layer with a thickness of 1.33 nm and slightly superior interface roughness in the range 0.3–0.6 nm. While the sample was kept at 120 °C, nitrogen was inserted in the chamber until the pressure reached 3.3×10^{-2} mbar. The chamber valves were then closed, keeping a static nitrogen pressure. The XRR measurements were performed continuously during the total treatment duration (48 h); however, few differences were observed between the curves. After 1 h of nitrogen treatment, the XRR curves were essentially identical to the curves obtained after annealing at 800 °C for 2 h. The surface still displayed only a NbO layer with a thickness of 1.33 nm. After 48 h in a nitrogen atmosphere, the thickness of the NbO layer decreased to 1.20 nm with similar interfacial roughness as the previous step, between 0.3 and 0.6 nm.

Interestingly, no evidence for either a nitrogen-rich or a nitride layer was observed with prolonged exposure of the Nb specimen to a nitrogen atmosphere at 120 °C, but rather only the progressive dissolution of the remaining NbO layer at the surface. For thin heteroepitaxial films, it is known that a passivating layer of NbO can be achieved after oxidation of Nb at 340 °C in a low-pressure dry oxygen atmosphere [33], which could in this case hinder nitrogen diffusion. Such a passivating layer was not present in the sample under test, as confirmed by the regrowth of the oxides NbO_2 and Nb_2O_5 after it was reexposed to air. Moreover, in contrast to what was observed for cavity-grade Nb upon high-temperature annealing, where rectangular- and triangular-shaped precipitates were observed at the surface [10,14], no precipitates were detected by SEM after infusion [see Fig. S1(a) in Supplemental Material [34]]. This indicates that the initial material purity may also play a role in the formation of such features on the surface.

Although SIMS measurements are difficult when dealing with nitrogen, as well as suffering from an inability to define the exact location of the oxide-metal interface [35], nitrogen incorporation in Nb after exposure to 3.3×10^{-2} mbar nitrogen at 120 °C [2,16] was reported. The reported concentrations should have been easily detectable by XRR measurements. One hypothesis to explain such discrepancies is the absence of grain boundaries in the samples studied in this work, which could act as enhanced diffusion sites for nitrogen atoms [36]. XPS results from the Nb 3d core level for polycrystalline Nb subjected to annealing cycles of 800 °C for 3 h in a high vacuum followed by 48 h at 140 °C with a nitrogen pressure of 3.3×10^{-2} mbar were interpreted as displaying $NbN_{(1-x)}O_x$ at a peak position of 203.2 eV [16]. Such a peak was also attributed by other authors [37,38] as belonging to NbC as well as NbO; therefore, an analysis

of the C 1s, N 1s, and O 1s core levels is necessary to understand the system fully. This is presented below.

C. Stepwise annealing and interstitial x-ray diffuse scattering

Interstitial atoms, such as oxygen and nitrogen, can occupy octahedral sites in the Nb bcc lattice [39,40]. Together with the natural mechanical instability along the [111] direction of the lattice leading to the ω phase [39,41], oxygen- and nitrogen-induced local distortions can produce diffuse scattering maxima at the reduced scattering vector $q^* = \frac{2}{3}(1\,1\,1)$ and space group Im-3m symmetry equivalent places in reciprocal space [23]. This diffracted intensity, in a regime of random defect concentration, can be written as [42]

$$I_D \propto c(1-c)S(\boldsymbol{Q}), \qquad (1)$$

where c is the concentration of the defect which is responsible for the intensity while $S(\boldsymbol{Q})$ is the square of the scattering amplitude of a single defect.

Contrary to the (110) surface, where the [111] direction resides in plane, for the (100) surface the diffuse maxima has an out-of-plane component. This makes the tuning of the x-ray exit angle impossible during the experiment. However, the probed depth can still be changed by modifying the x-ray incidence angle. Taking into account the sample curvature, it is possible to calculate an effective scattering depth (Λ_{eff}) for each measured step [24].

The evolution of the diffuse intensity was followed *in situ* during stepwise annealing in UHV (10^{-8} mbar) as well as in a nitrogen atmosphere. Starting from room temperature (RT), the sample was annealed at 120 °C, 200 °C, and 250 °C, sequentially. At 250 °C, nitrogen was inserted into the chamber until the pressure reached 3.3×10^{-2} mbar. Similar to the previous experiments, the N_2 atmosphere was kept under static conditions. Furthermore, the sample temperature was increased to 500 °C in the N_2 atmosphere as a last annealing step before air exposure. Together with diffuse scattering measurements, XRR curves were obtained for each temperature, providing information about the surface oxides. Table I summarizes the annealing temperatures and times at each step.

The thickness and roughness of the oxide layers during each step of annealing are presented in Fig. 4, while Fig. 5 shows the related *in situ* XRR curves and respective electron-density profiles extracted. The natural oxide layer was composed, beginning at the surface and ending at the metal-oxide interface, of Nb_2O_5, NbO_2, and NbO. The outermost oxide, Nb_2O_5, gradually decreased in thickness upon annealing up to 200 °C and vanished at 250 °C. Until 200 °C, NbO_2 followed the same trend as Nb_2O_5. However, upon further annealing it experiences a slight increase in thickness of about 0.09 nm, remaining almost constant thereafter. Hardly affected by annealing at 120 °C, NbO

TABLE I. Temperature, total time, and fitted decay lengths obtained by grazing incidence diffuse scattering measurements.

Temperature (℃)	Total time (hh:min)	Decay length (nm)
RT	. . .	0.969
120	13:45	0.989
200	14:00	1.970
250	15:20	2.713
$250 + N_2$	14:20	3.576
$500 + N_2$	10:00	. . .[a]

[a]Diffuse scattering measurements for the $500\,℃ + N_2$ annealing step are not discussed.

grows at the expense of the other oxides after annealing at 200 ℃ and starts to dissolve upon further annealing. The substrate roughness is barely affected by annealing at 120 ℃ and shows a steady growth as the temperature is increased. The stepwise dissolution of the natural oxides was also observed for the Nb(110) surface by both XPS and XRR measurements [28]. For the (110) surface, Nb_2O_5 dissolves faster than the other oxides (NbO_2 and NbO) at the surface, with its layer thickness decreasing $\sim$0.23 nm after annealing for 5 h in UHV at 145 ℃. On the other hand, as shown here, NbO_2 is consumed faster on the (100) surface, with a thickness decrease of $\sim$0.22 nm.

The behavior of the natural oxides proposed here is similar to what was observed in STM studies of the (100) surface, for which a reduction from Nb_2O_5 to NbO_2 was observed in the form of a ladderlike structure caused by oxygen segregation at the surface during annealing at 580 ℃ in UHV with subsequent regrowth of Nb_2O_5 after air exposure [43].

After N_2 exposure, no new nitride or nitrogen-rich layer was observed at 250 ℃, and the dissolution of the natural oxides has virtually stopped. However, at 500 ℃ a new layer with a thickness of 1.41 nm was formed between NbO
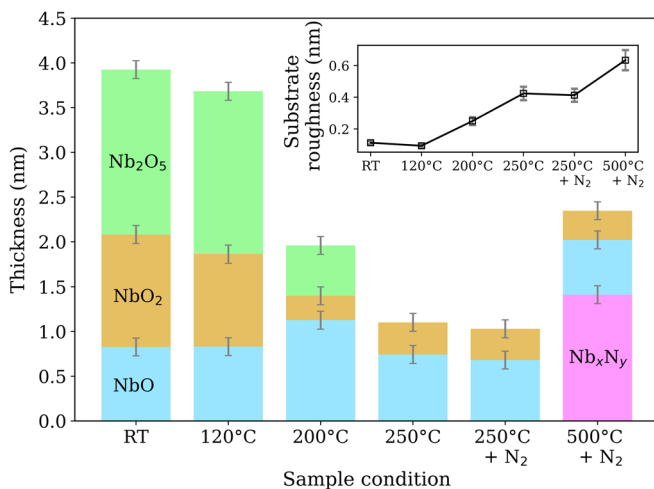
and Nb. The electron density of this layer is similar to the theoretically calculated value for the β-Nb_2N phase, which is known to precipitate upon high-temperature treatments in a N_2 atmosphere [10,14]. Therefore, it can be concluded that the layer relates to the presence of a possible Nb_xN_y compound underneath the oxide layer, as the presence of typical β-Nb_2N precipitates at the surface was not observed by SEM [Fig. S1(b) in Supplemental Material [34]].
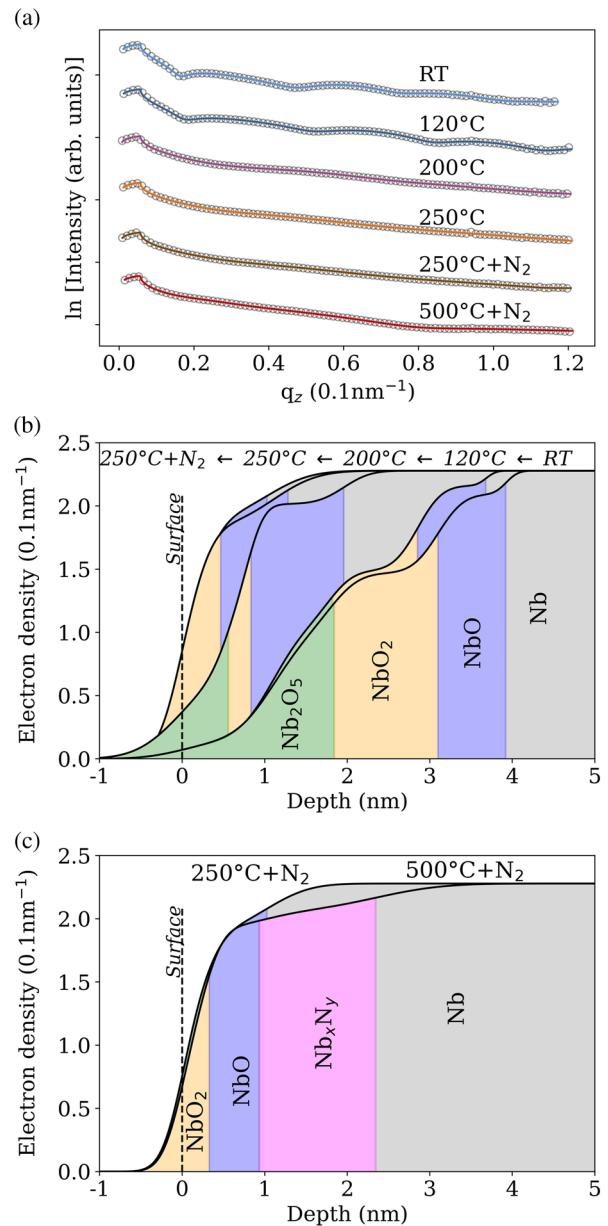

FIG. 5. (a) X-ray reflectivity data (open circles) measured with photon energies of 70 keV with the respective fits (solid lines). The scans are offset in the y direction. (b) Electron-density profiles obtained from the fits for the data collected from RT up to the addition of N_2 at 3.33×10^{-2} mbar at 250 ℃. (c) Comparison between the electron density profiles obtained at 250 ℃ and 500 ℃ in a N_2 atmosphere.

FIG. 4. Thickness and substrate roughness (inset) obtained by XRR in each step of the sample treatment.

During the high-energy GIXRD measurements, the sample is rotated around the Nb surface normal over 20° whereby the Nb hhl plane is swept through the Ewald sphere. The resulting diffraction patterns, obtained at different temperatures, are displayed in Fig. 6 for a fixed incident angle of 0.04°, corresponding to a scattering depth Λ_{eff} of ~100 nm. The detector is locally shielded by lead pieces at the strong Nb Bragg peak positions, which are labeled according to their hkl coordinates. Some powder rings from the beryllium window of the vacuum chamber are also visible. In between the Nb Bragg peaks, distinct diffuse scattering intensity is present. Close to the Bragg peaks, mostly thermal diffuse scattering (TDS) is observed, which grows in intensity with an increasing temperature. Oxygen and nitrogen interstitials give rise to pronounced diffuse scattering maxima near $Q = \frac{4}{3}(111)$ (see also Fig. 1). Clearly, at 120 °C, the overall diffuse scattering is very pronounced, and this is related to the dissolution of the native oxide layer and subsequent formation of oxygen interstitials.

In order to retrieve the depth-resolved concentration of the interstitials in the sample, a region of interest around $Q = \frac{4}{3}(111)$ ($\Delta q_{xy} = \Delta q_z = 0.42$ Å^{-1}) was analyzed in more detail. The integrated intensity in this area is evaluated as a function of the incident angle, which corresponds to a particular scattering depth Λ_{eff}. The resulting curve was fitted using an exponential decay model for the interstitial concentration such as

$$c(z) = ae^{(-z-z_0)/\tau} + d, \quad \text{for } z < z_0, \tag{2}$$

where the fitted parameters are a preexponential factor a, giving the excess concentration at the interface, an exponential decay length τ, and a final bulk concentration d. z is the depth, with zero being the vacuum-oxide interface and z_0 the position of the metal-oxide interface. The values of a and d are concentrations given in terms of the ratio between the number of defects N_D and the total number of atoms N_T. Thermal diffuse-scattering contributions as well as optical factors [24,26] were also taken into account by the fitting routine.

Figure 7(a) shows the diffuse scattering data collected from RT up to 250 °C in a N$_2$ atmosphere. The interstitial concentration profile extracted from the fits is presented in Fig. 7(b). An increase in the decay length of subsurface oxygen, associated with a decrease of the initial concentration (at $z = 0$), was observed as the temperature was increased, as seen in the inset in Fig. 7(b). This behavior can be understood as the progressive diffusion of oxygen liberated from the oxide layers, which in turn decrease in total thickness. Furthermore, as the temperature increases, the diffusion length of the liberated oxygen in Nb increases drastically. The interstitial concentration in the first 10 nm is the highest during annealing at 120 °C, which agrees with the 12 nm of calculated diffusion length of oxygen in pure Nb [17]. Compared to 120 °C, annealing at 200 °C liberates more oxygen in the Nb matrix and enables it to diffuse
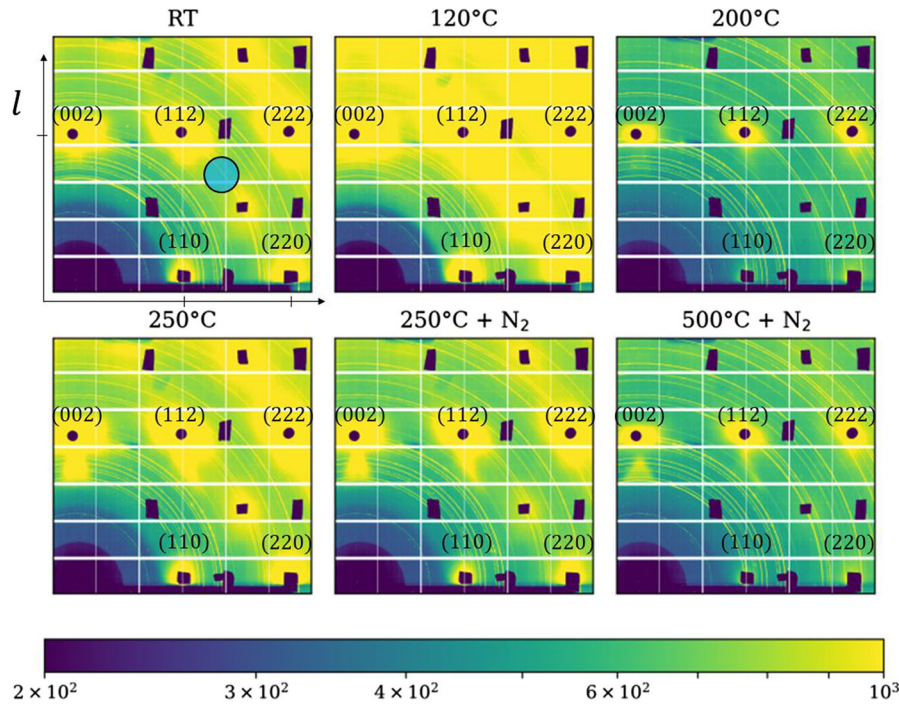

FIG. 6. Diffraction patterns obtained at different temperatures with an incident angle of 0.04°, corresponding to a scattering depth Λ_{eff} of ~100 nm. At 120 °C, a clear increase in diffuse intensity is observed due to the presence of subsurface oxygen. Lead (Pb) pieces block the Nb Bragg peaks. Powder rings originating from the beryllium (Be) windows of the chamber are also observed. The region of interest employed in the data analysis is schematically shown in blue (see the text for details).
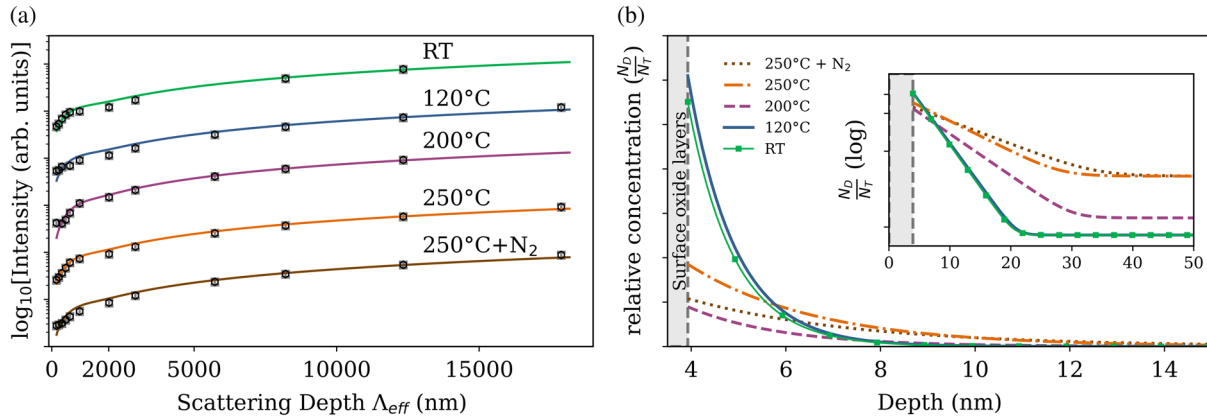
FIG. 7.   (a) Diffuse scattering intensities obtained for each temperature step (squares) and the respective fit (solid line). The curves are offset in the *y* direction. (b) Interstitial concentration obtained from the fit plotted in the linear scale and the concentration in the log scale (inset). The profiles are represented by connected squares (room temperature), solid (120 °C), dashed (200 °C), dot-dashed (250 °C), and dotted lines (250 °C under a N_2 atmosphere).

further. This is seen by the increase in the bulk concentration from $\sim 3 \times 10^{-9}$ to $\sim 3 \times 10^{-8}$ as well as the decay-length increase from 0.98 to 1.97 nm. On the other hand, the subsurface concentration in the first tens of nanometers decreases. The same trend continued during annealing at 250 °C, increasing even more the decay length up to 2.71 nm and the bulk concentration to $\sim 5 \times 10^{-6}$. The total number of interstitials is determined by the availability of oxygen and nitrogen species. The XRR results indicate that the dissolution rate of the oxides has decreased considerably after the first annealing step to 250 °C, and it is concluded that this process has nearly ended. Therefore, the number of interstitials diffusing into the bulk from the near-surface region is higher than the influx from the surface. Hence, the interstitial concentration within the first few nanometers decreased, while the decay length increased to 3.57 nm. The concentration in the large bulk reservoir remained essentially the same. This means that annealing in a N_2 atmosphere at 250 °C promoted only further diffusion of oxygen originating from the surface oxides into Nb with no evidence of nitrogen incorporation in the metallic Nb matrix. The corresponding decay lengths for different annealing steps are summarized in Table I.

High-resolution XPS measurements were performed after the sample was reexposed to air for 10 days. Deconvoluted XPS spectra of Nb 3d observed for the normal, as well as the grazing-exit mode, are shown in Figs. 8(a) and 8(b), which confirm the regrowth of the natural oxide layers previously partially dissolved due to the stepwise UHV annealing. The characteristic doublets of metallic Nb are observed at the binding energies of 202.0 and 204.7 eV. The top surface oxide layer on Nb is consisting of Nb_xO, NbO, NbO_2, and Nb_2O_5, for which the binding energies exceed to metallic Nb by 0.7, 1.9, 3.0, and 5.0 eV, respectively. A strong contribution from NbC is suggested by the presence of $3d_{5/2}$ and $3d_{3/2}$ peaks at

203.3 and 206.0 eV, respectively, and confirmed by the presence of a peak in C 1s core level at 282.6 eV assigned to the Nb—C bond [44] (Fig. S2 in Supplemental Material [34]). Furthermore, a contribution from two peaks at binding energies of 204.3 and 207.0 eV is detected, which can be attributed to a NbN_xO_y phase, supported by the presence of a peak in N 1s core level [Figs. 8(c) and 8(d)] at the binding energy of ~ 397.5 eV, which corresponds to Nb bound to N in niobium nitrides and oxynitrides as reported for the nitrogen-doped niobium samples [10]. The peak at a higher binding energy in the N 1s region at ~ 400 eV is assigned to the adsorbed N on the surface. The intensity of the lower binding energy peak in the N 1s spectrum is
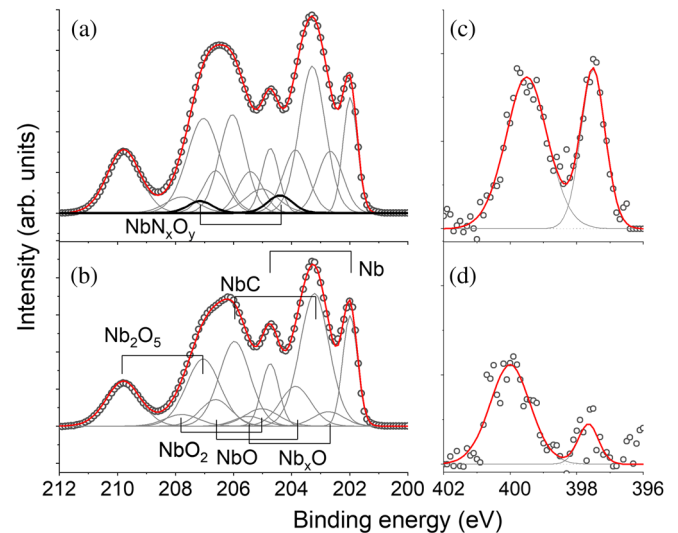

FIG. 8.   Deconvolution of Nb 3d and N 1s lines in normal exit mode (a),(c) and with a 70° exit angle (b),(d). Phases corresponding to niobium, niobium oxides, and niobium carbides are represented in gray. Contributions from niobium nitrides are shown in black.

significantly suppressed when measured at the grazing-exit angle given in Fig. 8(d), where the majority of detected photoelectrons correspond to the top surface layer. Moreover, the peaks corresponding to the NbN_xO_y phase in the normal-exit Nb 3d spectrum in Fig. 8(a) are not observable in the grazing-exit Nb 3d spectrum in Fig. 8(b). These results indicate that the nitrogen-containing phase does not reside on the top layer but close to the oxide-metal interface, which is in line with the *in situ* XRR measurements on the same sample at 500 °C in a nitrogen atmosphere.

IV. CONCLUSIONS

The effect of different thermal treatments that have been recently applied to Nb SRF cavities was studied in the near-surface region of single-crystalline Nb(100). *In situ* XRR revealed that annealing to 800 °C in UHV reduces the natural oxide layer composed of Nb_2O_5, NbO_2, and NbO into solely NbO; the natural oxide layer was observed to regrow after exposure to air. After a nitrogen exposure at 120 °C and 3.3×10^{-2} mbar, neither a nitrogen-rich layer nor interstitial nitrogen were detected. *In situ* high-energy x-ray diffuse scattering combined with XRR measurements during stepwise annealing in UHV up to 250 °C demonstrated that the partial dissolution of the natural oxides leads to the diffusion of oxygen into Nb. At 120 °C, interstitial oxygen is mostly present within the first 10 nm, while a temperature increase leads to further diffusion into the *bulk*. When the sample was exposed to 3.3×10^{-2} mbar of N_2 at 250 °C, no evidence of nitrogen presence either in the form of a nitrogen-containing layer or as interstitial nitrogen was detected. Annealing at 500 °C resulted in the formation of a Nb_xN_y layer underneath the remaining NbO_2 and NbO at

the surface. A schematic representation of the stepwise procedure is shown in Fig. 9.

Ex situ photoelectron spectroscopy measurements confirm the presence of Nb-N bonding as well as the regrowth of the natural oxide layer at the surface upon exposure to air. These results suggest that higher-temperature treatments (e.g., above 250 °C) are necessary for nitrogen to react effectively for the case of the ideal situation of ultrapure Nb single crystals, in line with Nb-N thermodynamics. In turn, we may conclude that the nitrogen-induced increased performance of SRF cavities after low-temperature annealing is related to real cavity material properties such as grain boundaries and its higher level of impurities, such as carbon. A rearrangement of the oxygen interstitial profile takes place during the low-temperature annealing of Nb in a nitrogen atmosphere, which is suggested in the literature to be potentially partially responsible for cavity improvements [2]. Further studies concerning the effect of grain boundaries as well as other crystal orientations are recommended in order to elucidate the apparent improvement in the performance of SRF cavities subjected to low-temperature thermal treatments.
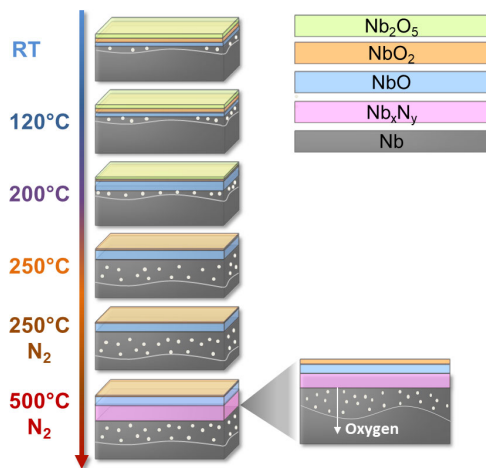
FIG. 9. Schematic representation of the stepwise annealing of Nb(100). The natural oxide layers gradually dissolve, and the liberated oxygen atoms diffuse into the Nb matrix. At 500 °C under a N_2 atmosphere, a Nb_xN_y layer is formed underneath the remaining niobium oxides.

[1] D. Reschke, V. Gubarev, J. Schaffran, L. Steder, N. Walker, M. Wenskat, and L. Monaco, Performance in the vertical test of the 832 nine-cell 1.3 GHz cavities for the European X-ray Free Electron Laser, Phys. Rev. Accel. Beams **20,** 042004 (2017).

[2] A. Grassellino, A. Romanenko, Y. Trenikhina, M. Checchin, M. Martinello, O. S. Melnychuk, S. Chandrasekaran, D. A. Sergatskov, S. Posen, A. C. Crawford, S. Aderhold, and D. Bice, Unprecedented quality factors at accelerating gradients up to 45 MVm−1 in niobium superconducting resonators via low temperature nitrogen infusion, Supercond. Sci. Technol. **30,** 094004 (2017).

[3] A. Grassellino, A. Romanenko, D. Sergatskov, O. Melnychuk, Y. Trenikhina, A. Crawford, A. Rowe, M. Wong, T. Khabiboulline, and F. Barkov, Nitrogen and argon doping of niobium for superconducting radio frequency cavities: a pathway to highly efficient accelerating structures, Supercond. Sci. Technol. **26,** 102001 (2013).

[4] J. T. Maniscalco, D. Gonnella, and M. Liepe, The importance of the electron mean free path for superconducting radio-frequency cavities, J. Appl. Phys. **121,** 043910 (2017).

[5] M. Martinello, A. Grassellino, M. Checchin, A. Romanenko, O. Melnychuk, D. A. Sergatskov, S. Posen, and J. F. Zasadzinski, Effect of interstitial impurities on the field dependent microwave surface resistance of niobium, Appl. Phys. Lett. **109**, 062601 (2016).

[6] Y. Trenikhina, A. Romanenko, J. Kwon, J.-M. Zuo, and J. F. Zasadzinski, Nanostructural features degrading the performance of superconducting radio frequency niobium cavities revealed by transmission electron microscopy and electron energy loss spectroscopy, J. Appl. Phys. **117**, 154507 (2015).

[7] F. Barkov, A. Romanenko, and A. Grassellino, Direct observation of hydrides formation in cavity-grade niobium, Phys. Rev. Accel. Beams **15**, 122001 (2012).

[8] W. Singer, A. Brinkmann, R. Brinkmann, J. Iversen, A. Matheisen, W.-D. Moeller, A. Navitski, D. Reschke, J. Schaffran, A. Sulimov, N. Walker, H. Weise, P. Michelato, L. Monaco, C. Pagani, and M. Wiencek, Production of superconducting 1.3-GHz cavities for the European X-ray Free Electron Laser, Phys. Rev. Accel. Beams **19**, 092001 (2016).

[9] J. Knobloch, The "Q disease" in superconducting niobium RF cavities, AIP Conf. Proc. **671**, 133 (2003).

[10] A. Dangwal Pandey, G. Dalla Lana Semione, A. Prudnikava, T. F. Keller, H. Noei, V. Vonk, Y. Tamashevich, E. Elsen, B. Foster, and A. Stierle, Surface characterization of nitrogen-doped Nb (100) large-grain superconducting RF cavity material, J. Mater. Sci. **53**, 10411 (2018).

[11] A. V. Linde, R.-M. Marin-Ayral, D. Granier, F. Bosc-Rouessac, and V. V. Grachev, Synthesis of cubic niobium nitride by reactive diffusion under nitrogen pressure, Mater. Res. Bull. **44**, 1025 (2009).

[12] A. H. Farha, O. M. Ozkendir, H. E. Elsayed-Ali, G. Myneni, and Y. Ufuktepe, The effect of heat treatment on structural and electronic properties of niobium nitride prepared by a thermal diffusion method, Surf. Coat. Technol. **309**, 54 (2017).

[13] Y. Ufuktepe, A. H. Farha, S. I. Kimura, T. Hajiri, K. Imura, M. A. Mamun, F. Karadag, A. A. Elmustafa, and H. E. Elsayed-Ali, Superconducting niobium nitride thin films by reactive pulsed laser deposition, Thin Solid Films **545**, 601 (2013).

[14] Y. Ufuktepe, A. H. Farha, S. Kimura, T. Hajiri, F. Karadağ, M. A. Al Mamun, A. A. Elmustafa, G. Myneni, and H. E. Elsayed-Ali, Structural, electronic, and mechanical properties of niobium nitride prepared by thermal diffusion in nitrogen, Mater. Chem. Phys. **141**, 393 (2013).

[15] B. An, M. Xu, S. Fukuyama, and K. Yokogawa, Nitrogen-induced structures of a Nb(100) surface investigated by LEED, Auger electron spectroscopy, and STM, Phys. Rev. B **73**, 205401 (2006).

[16] P. Dhakal, S. Chetri, S. Balachandran, P. J. Lee, and G. Ciovati, Effect of low temperature baking in nitrogen on the performance of a niobium superconducting radio frequency cavity, Phys. Rev. Accel. Beams **21**, 032001 (2018).

[17] E. Fromm and E. Gebhardt, *Gase Und Kohlenstoff in Metallen* (Springer-Verlag, Berlin, 1976).

[18] M. Lohmeier and E. Vlieg, Angle calculations for a six-circle surface X-ray diffractometer, J. Appl. Crystallogr. **26**, 706 (1993).

[19] E. Vlieg, Integrated intensities using a six-circle surface x-ray diffractometer, J. Appl. Crystallogr. **30**, 532 (1997).

[20] A. Stierle, T. F. Keller, H. Noei, V. Vonk, and R. Roehlsberger, DESY NanoLab, J. Large-Scale Res. Facil. **2**, A76 (2016).

[21] U. Hejral, P. Müller, M. Shipilin, J. Gustafson, D. Franz, R. Shayduk, U. Rütt, C. Zhang, L. R. Merte, E. Lundgren, V. Vonk, and A. Stierle, High-energy x-ray diffraction from surfaces and nanoparticles, Phys. Rev. B **96**, 195433 (2017).

[22] H. Reichert and V. Honkimäki, in *Synchrotron Light Sources Free. Lasers* (Springer, Cham, 2016), pp. 1557–1577.

[23] H. Dosch and J. Peisl, Unusual diffuse scattering intensities from nitrogen in niobium, Phys. Rev. B **32**, 623 (1985).

[24] H. Dosch, *Critical Phenomena at Surfaces and Interfaces: Evanescent X-Ray and Neutron Scattering* (Springer-Verlag, Berlin, 1992).

[25] H. Dosch, Evanescent absorption in kinematic surface Bragg diffraction, Phys. Rev. B **35**, 2137 (1987).

[26] H. Dosch, B. W. Batterman, and D. C. Wack, Depth-Controlled Grazing-Incidence Diffraction of Synchrotron X Radiation, Phys. Rev. Lett. **56**, 1144 (1986).

[27] P. Dhakal, G. Ciovati, P. Kneisel, and G. R. Myneni, Enhancement in quality factor of SRF niobium cavities by material diffusion, IEEE Trans. Appl. Supercond. **25**, 1 (2015).

[28] M. Delheusy, A. Stierle, N. Kasper, R. P. Kurta, A. Vlad, H. Dosch, C. Antoine, A. Resta, E. Lundgren, and J. Andersen, X-ray investigation of subsurface interstitial oxygen at Nb/oxide interfaces, Appl. Phys. Lett. **92**, 101911 (2008).

[29] J. M. Dickey, H. H. Farrell, O. F. Kammerer, and M. Strongin, Surface studies on niobium and some implications for superconductivity, Phys. Lett. A **32**, 483 (1970).

[30] A. B. Odobesko, S. Haldar, S. Wilfert, J. Hagen, J. Jung, N. Schmidt, P. Sessi, M. Vogt, S. Heinze, and M. Bode, Preparation and electronic properties of clean superconducting Nb(110) surfaces, Phys. Rev. B **99**, 115437 (2019).

[31] Q. Ma, P. Ryan, J. W. Freeland, and R. A. Rosenberg, Thermal effect on the oxides on Nb(100) studied by synchrotron-radiation x-ray photoelectron spectroscopy, J. Appl. Phys. **96**, 7675 (2004).

[32] C. Varmazis, A. Joshi, T. Luhman, and M. Strongin, Effect of high-temperature heat treatment on penetration depth of superconducting niobium, Appl. Phys. Lett. **24**, 394 (1974).

[33] O. Hellwig, H. W. Becker, and H. Zabel, Ordered oxygen phases in epitaxial Nb(110) layers, Phys. Rev. B **64**, 233404 (2001).

[34] See Supplemental Material at http://link.aps.org/supplemental/10.1103/PhysRevAccelBeams.22.103102 for SEM images and XPS measurements of C 1s core level.

[35] C. Antoine, Materials and Surface Aspects in the Development of SRF Niobium Cavities, EuCARD Editorial Series on Accelerator Science and Technology (EuCARD, 2012).

[36] C. Herzig and Y. Mishin, in *Diffusion in Condensed Matter* (Springer-Verlag, Berlin, 2005), pp. 337–366.

[37] M. T. Marques, A. M. Ferraria, J. B. Correia, A. M. B. do Rego, and R. Vilar, XRD, XPS and SEM characterisation

of Cu–NbC nanocomposite produced by mechanical alloying, Mater. Chem. Phys. **109**, 174 (2008).

[38] A. Daccà, G. Gemme, L. Mattera, and R. Parodi, XPS analysis of the surface composition of niobium for super-conducting RF cavities, Appl. Surf. Sci. **126**, 219 (1998).

[39] H. Dosch, A. v. Schwerin, and J. Peisl, Point-defect-induced nucleation of the ω phase, Phys. Rev. B **34**, 1654 (1986).

[40] M. S. Blanter and A. G. Khachaturyan, Stress-induced interaction of pairs of point defects in bcc solutions, Metall. Trans. A **9**, 753 (1978).

[41] R. P. Kurta, V. N. Bugaev, A. Stierle, and H. Dosch, Incommensurate strain-induced ordering of interstitial oxygen in Nb, J. Phys. Condens. Matter **20**, 275206 (2008).

[42] M. A. Krivoglaz, V. G. Baryakhtar, M. A. Ivanov, S. C. Moss, and J. Peisl, *X-Ray and Neutron Diffraction in Nonideal Crystals* (Springer, Berlin, 1996).

[43] Y. Li, B. An, S. Fukuyama, K. Yokogawa, and M. Yoshimura, Surface oxidation of a Nb(100) single crystal by scanning tunneling microscopy, Mater. Charact. **48**, 163 (2002).

[44] A. Darlinski and J. Halbritter, Angle-resolved XPS studies of oxides at NbN, NbC, and Nb surfaces, Surf. Interface Anal. **10**, 223 (1987).